



ARTICLE

<https://doi.org/10.1038/s41467-019-12599-3>

OPEN

Non-reciprocal robotic metamaterials

Martin Brandenbourger¹, Xander Locsin¹, Edan Lerner¹  & Corentin Coulais^{1*} 

Non-reciprocal transmission of motion is potentially highly beneficial to a wide range of applications, ranging from wave guiding to shock and vibration damping and energy harvesting. To date, large levels of non-reciprocity have been realized using broken spatial or temporal symmetries, yet mostly in the vicinity of resonances, bandgaps or using nonlinearities, thereby non-reciprocal transmission remains limited to narrow ranges of frequencies or input magnitudes and sensitive to attenuation. Here, we create a robotic mechanical metamaterials wherein we use local control loops to break reciprocity at the level of the interactions between the unit cells. We show theoretically and experimentally that first-of-their-kind spatially asymmetric standing waves at all frequencies and unidirectionally amplified propagating waves emerge. These findings realize the mechanical analogue of the non-Hermitian skin effect. They significantly advance the field of active metamaterials for non hermitian physics and open avenues to channel mechanical energy in unprecedented ways.

¹Institute of Physics, Universiteit van Amsterdam, Science Park 904, 1098 XH Amsterdam, The Netherlands. *email: coulais@uva.nl

Reciprocity is a fundamental property of linear, time-reversal invariant physical systems, entailing that their response functions are symmetrical, namely that signals are transmitted symmetrically between any two points in space^{1–3}. In other words, if one sends an electromagnetic, acoustic, or mechanical signal through a material in one direction, one can also send it in the opposite direction. While breaking reciprocity has been a long-standing challenge in electromagnetics, there has been over the last few years an explosion of interest for breaking reciprocity in optical^{4–7} and micro⁸ waves without magnetic fields, and beyond electromagnetism, i.e., in acoustics⁹, quantum systems^{10,11}, and mechanics^{12,13}, thus creating new tools to engineer a novel generation of devices and materials that guide, damp, or control energy and information. Non-reciprocity has been achieved by using passive structures combining broken spatial symmetries and nonlinearities^{13,14} and using active time-modulated components that break time-reversal symmetry^{3,12,15–17}. These strategies have led to large levels of nonreciprocal isolations, but with input magnitudes or input frequencies that are limited to narrow ranges, and are sensitive to attenuation.

Here, inspired by recent developments in robotics^{18,19} and active metamaterials^{12,16,17,20–22}, we create a robotic mechanical metamaterial that uses distributed active control to break reciprocity at the level of the interactions between the building blocks themselves. This work builds on the field of active metamaterials, yet with a key new twist: while active metamaterials only have actuating elements, robotic metamaterials include a combination of local sensing, computation, communication, and actuation. As a result, they feature unique wave phenomena, namely asymmetric modes at all frequencies and unidirectional amplification, and in turn realize large, broadband, linear, and self-amplified nonreciprocal transmission of mechanical waves. These findings realize the classical counterpart of the so-called non-Hermitian skin effect^{23–28}.

Results

Nonreciprocal wave equation. We first investigate theoretically the emergent properties in a mass-and-spring model with nonreciprocal springs (Fig. 1a). For reciprocal mechanical

structures^{1,29,30}, the stiffness matrix—relating displacements to forces—is symmetrical by virtue of the Maxwell–Betti reciprocity theorem¹. In particular, for a simple spring, left-to-right and right-to-left stiffnesses are equal: $k_{L\rightarrow R} = k_{R\rightarrow L} = k$ where $k_{L\rightarrow R}$ and $k_{R\rightarrow L}$ are defined as $k_{L\rightarrow R} = F_{L\rightarrow R}/(u_R - u_L)$ and $k_{R\rightarrow L} = F_{R\rightarrow L}/(u_L - u_R)$, where F_L (F_R) is the force on the left (right) spring and u_L (u_R) the displacement of the left (right) spring. Here, we consider a special mass-and-spring model, where the left-to-right and right-to-left stiffnesses differ $k_{L\rightarrow R} = k(1 + \varepsilon) \neq k_{R\rightarrow L} = k(1 - \varepsilon)$ (Fig. 1a). We obtain the following continuum equation (Methods, Mass-and-spring model with nonreciprocal springs)

$$\frac{1}{c^2} \frac{d^2 u}{dt^2} - \frac{d^2 u}{dx^2} + \frac{2\varepsilon}{p} \frac{du}{dx} = 0, \quad (1)$$

where $c = p\sqrt{k/m}$ and where p is the interparticle distance. In the case of reciprocal interactions ($\varepsilon = 0$), Eq. (1) becomes the wave equation, which admits dispersion-free mechanical waves of group and phase velocity c . For nonreciprocal interactions ($\varepsilon \neq 0$), the first-order term in Eq. (1) breaks inversion symmetry $u \rightarrow -u$, $x \rightarrow -x$. This asymmetry has dramatic consequences on the nature of the mechanical waves, which can be readily seen from the solutions of this equation both in the frequency domain and in real space. In the frequency domain, solutions consist of a linear combination of the functions $\exp(i(\omega t - q_{\pm} x))$, where the wave vector $q_{\pm} = \frac{i}{p}(\varepsilon \pm \sqrt{\varepsilon^2 - \omega^2 p^2 / c^2})$. For small frequencies $\omega < c|\varepsilon|/p$, these solutions are exponentially localized standing waves, while for large frequencies $\omega > c|\varepsilon|/p$, they are localized oscillatory standing waves with an exponential envelope (Fig. 1b). Crucially, for $\varepsilon > 0$ ($\varepsilon < 0$), the imaginary part is always positive (negative), so these solutions are always localized on the right (left) edge. In real space, we obtain the Green's function of Eq. (1) (Methods, Mass-and-spring model with nonreciprocal springs and Supplementary Information Note 1), which is an asymmetric step function propagating at a velocity c with a wave front magnitude given by $\exp(\varepsilon ct/p)/2$ ($\exp(-\varepsilon ct/p)/2$) for $x > 0$ ($x < 0$). For any value of $\varepsilon > 0$ ($\varepsilon < 0$), the initial pulse is amplified for forward (backward) propagation and attenuated for backward (forward) propagation (Fig. 1c). This behavior can be intuitively understood from the structure of Eq. (1): work is injected in

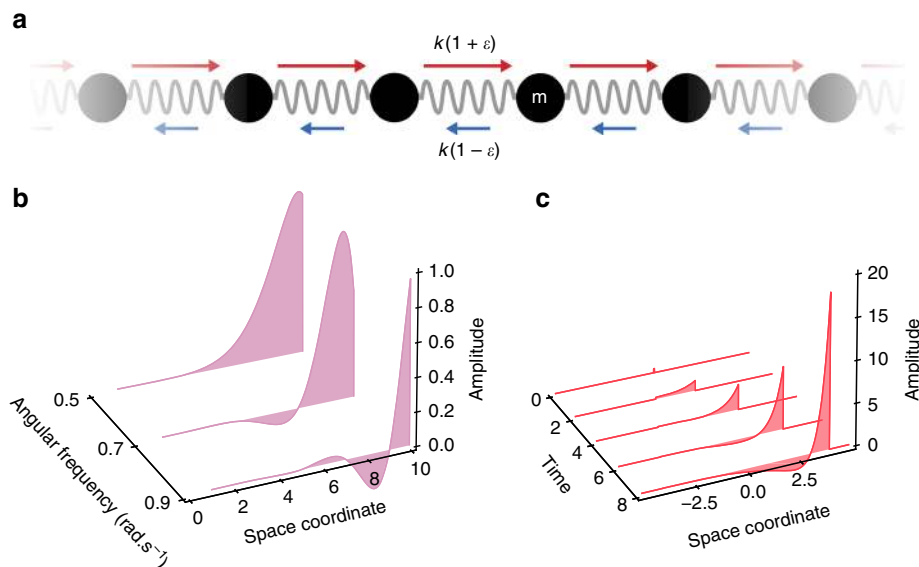


Fig. 1 Asymmetric and unidirectionally amplified waves in a nonreciprocal mass-and-spring model. **a** Schematic representation of the nonreciprocal mass-and-spring model. **b** Magnitude of the solutions of Eq. (1) in the frequency domain $\exp(i(\omega t - q_{\pm} x))$ vs. spatial coordinate, for three different frequencies. **c** Green's function of Eq. (1) vs. time and spatial coordinate. In **(b)** and **(c)**, $\varepsilon = 0.9$ and $c = 0.5$

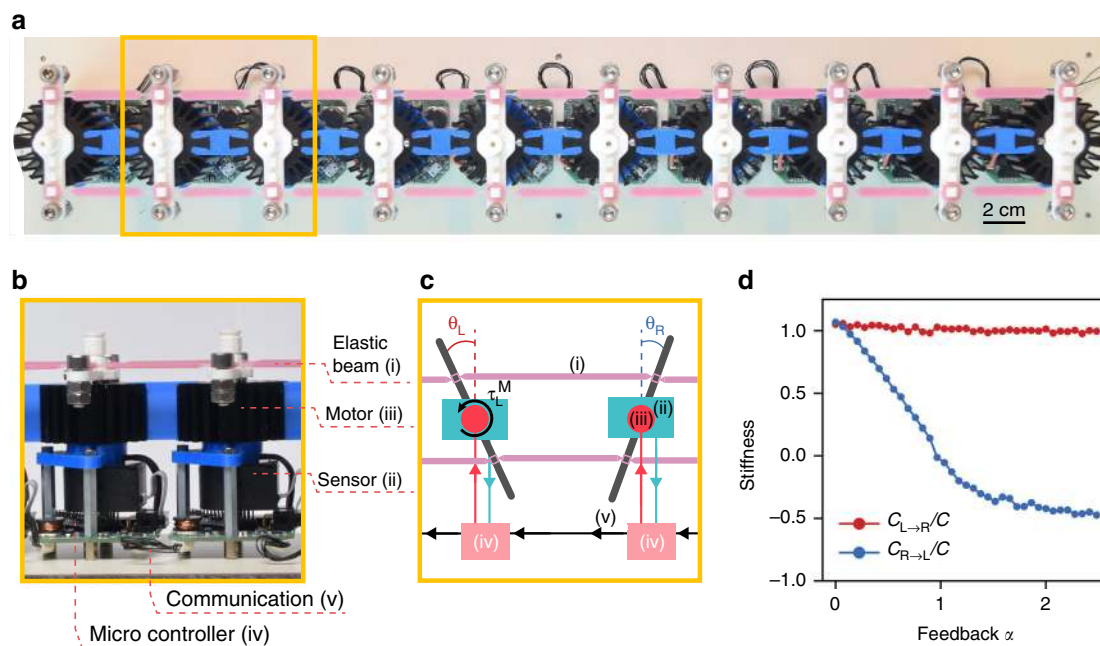


Fig. 2 Robotic metamaterial with nonreciprocal interactions. **a** Robotic metamaterial made of 10 unit cells mechanically connected by soft elastic beams (i). Scale bar: 2 cm. (bc) Closeup **b** and sketch **c** on two unit cells. Each unit cell is a minimal robot with a unique rotational degree of freedom that comprises an angular sensor (ii), a coreless DC motor (iii), and a microcontroller (iv). Each unit cell communicates with its right neighbor via electric wires (v). These components allow to program a control loop characterized by the feedback parameter α (see main text for definition). **d** Rescaled torsional stiffnesses $C_{L \rightarrow R}/C$ (red) and $C_{R \rightarrow L}/C$ (blue) as a function of the feedback parameter

(extracted from) the wave front when $\frac{2\varepsilon}{p} \frac{du}{dx}$ is negative (positive), whereby the system is constantly driven out-of-equilibrium. This leads to waves with two unprecedented features, namely spatial asymmetry at all frequencies and unidirectional amplification.

Nonreciprocal robotic metamaterial. In order to create a system with such effective nonreciprocal local interactions, a necessary but not sufficient condition is to add external forces. Our strategy for achieving such nonreciprocal interactions is to apply strain-dependent forces at each site, i.e., forces that are proportional to the strain in the neighboring springs²². These local forces inject—linear or angular—momentum and work into the mechanical degrees of freedom. To do so, we built a metamaterial made of ten “robotic” building blocks (Fig. 2a) with rotational degrees of freedom. Each robotic unit cell consists of a mechanical rotor with a rotational moment of inertia J , of a local control system, and is mechanically coupled to its neighbors via pre-stretched elastic beams resulting in a torsional stiffness C (Fig. 2b, c). The control system measures the rotor’s angular position θ_L , collects that of its right neighbor θ_R , and applies an additional torque on the left rotor $\tau_M = Cf(\alpha)(\theta_L - \theta_R)$. The parameter α is a dimensionless feedback parameter. The feedback gain $f(\alpha)$ plays a similar role as the parameter ε in the model of Fig. 1, yet with a subtle difference. In the experiment, the active force is applied only on the right neighbor, whereas in the model, the active force is applied on both left and right neighbors (Methods, Mass-and-spring model with nonreciprocal springs). We calibrate the torque vs. angle response between two unit cells and find, as expected, that $C_{L \rightarrow R} = C$ differs from $C_{R \rightarrow L} = C(1 - f(\alpha))$ (Fig. 2d), therefore breaking reciprocity. While such tunable nonreciprocal response is not surprising—ultimately it is achieved at the level of each unit cell’s microcontroller—the novelty of our approach lies in coupling many such robotic nonreciprocal unit cells together and making use of the fact that the bandwidth of

the electronic components is much larger than that of the mechanical degrees of freedom. As a result of the interaction between multiple robotic building blocks, unique nonreciprocal wave phenomena emerge, as we will see in the following sections.

To test the predictions of the mass-and-spring model, we now investigate experimentally and numerically the stationary response of our ten-unit cells robotic metamaterial to harmonic excitations on the left and on the right edges over a wide range of input frequencies (Methods, Calibration and measurements). In the reciprocal case $\alpha = 0$ (Fig. 3a), we observe from experiments that the amplitudes of oscillation of each unit cell either decay exponentially (low frequencies) or oscillate (high frequencies) from one unit cell to another. We model the robotic metamaterial as 10 coupled oscillators interacting with each other via nonreciprocal stiffnesses $C_{L \rightarrow R}$ and $C_{R \rightarrow L}$. To do so, we take into account additional effects such as the bending of the rubber bands and the inherent damping of the oscillators and quantify them via independent calibration (Methods, Calibration and measurements). The model matches the observations very accurately without any fit parameters until 3 Hz, above which the numerical model is too simplistic to accurately capture internal vibrations of the rubber bands (Methods, Numerical model of the robotic metamaterial). For all actuation frequencies, we observe from the model and the experiment that the responses to left and right excitations is simply related to mirror symmetry, which demonstrates that the metamaterial response is inherently symmetrical. In contrast, in the nonreciprocal case $\alpha = 0.43$ (Fig. 3b), we observe a strong asymmetry in the angular displacement profiles. When excited from the right, the response is more localized close to the excitation point and when excited from the left, the response is more extended toward the right and even increases for large frequencies. This asymmetry is further quantified by the spatial decays of the profiles, which are opposite in the reciprocal case $\alpha = 0$ (Fig. 3c) and differ in the nonreciprocal case $\alpha = 0.43$ (Fig. 3d), regardless of the driving frequency. Figure 3d therefore demonstrates the emergence of

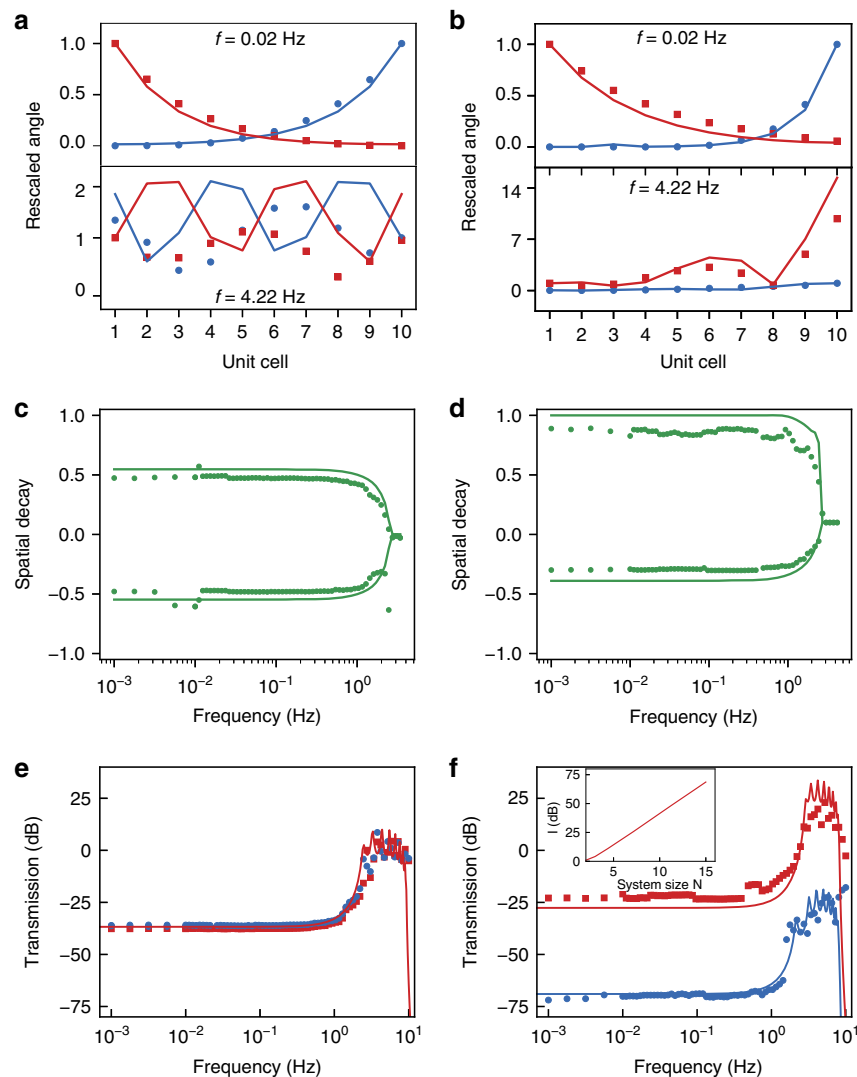


Fig. 3 Spatially asymmetric standing waves and broadband unidirectional transmission. Stationary response under sinusoidal excitations at the left (red squares) or right (blue dots) edge of the metamaterial. (ab) Amplitudes of oscillation rescaled by the amplitude of actuation as a function of the unit cell position for sinusoidal excitations with $\alpha = 0$ (a) and $\alpha = 0.43$ (b) at frequencies 0.02 Hz (top) and 4.22 Hz (bottom). See also Supplementary Video 1. (cd) Spatial decay rates of the amplitudes of oscillation vs. frequency with $\alpha = 0$ (c) and $\alpha = 0.43$ (d). (ef) Left-to-right ($T_{L \rightarrow R}$) and right-to-left ($T_{R \rightarrow L}$) transmissions as a function of the excitation frequency (f) for a feedback parameter $\alpha = 0$ (e) and $\alpha = 0.43$ (f). (f-inset) Isolation at low frequency $I = T_{L \rightarrow R} - T_{R \rightarrow L}$ as a function of the number of unit cells N , for $\alpha = 0.43$. For each graph, markers depict the experiments and solid lines the numerical model. Note that beyond 10 Hz our experimental system cannot drive and measure

asymmetric modes at all frequencies, as predicted by the solutions of Eq. (1) and reminiscent of the non-Hermitian skin effect^{23–28}.

Does such strong asymmetry lead to nonreciprocal transmission? To address this question, we calculate the transmissions $T_{L \rightarrow R} = 20 \log_{10} |\hat{\theta}_R^{\text{out}} / \hat{\theta}_L^{\text{in}}|$ and $T_{R \rightarrow L} = 20 \log_{10} |\hat{\theta}_L^{\text{out}} / \hat{\theta}_R^{\text{in}}|$ for various frequencies from the angular displacement profiles obtained above. In the reciprocal case ($\alpha = 0$), we observe a symmetrical transmission, typical of a resonant low-pass filter, with a saturated plateau of amplitude -37 ± 1 dB at small frequencies and a broad peak corresponding to the system resonances beyond which the transmission signal starkly decreases at 360 dB/decade (Fig. 3e). For the nonreciprocal case ($\alpha = 0.43$), the left-to-right and right-to-left transmissions differ vastly—by more than 50 dB—over a wide range of frequencies, from 0.001 to 5 Hz (Fig. 3f). Strikingly, as opposed to previous observations in mechanical metamaterials whose functionality decays with system size^{31,32}, such nonreciprocal isolation increases linearly with the system size (Fig. 3f—inset). Therefore, the isolation of the system can be controlled by

varying the feedback α or by adding more unit cells, the latter having the advantage of avoiding limitations in the maximal torque applied by the control loop. Importantly, our metamaterial is linearly stable over a wide range of feedback parameters ($\alpha < 0.93$) (Methods, Numerical model of the robotic metamaterial). Therefore, the existence of the asymmetric modes at all frequencies leads to an extremely large level of nonreciprocal transmission over a very large range of frequencies, a performance that is unprecedented among wave-based physical systems.

Since the nonreciprocal transmission is broadband, our robotic metamaterial is in principle an excellent nonreciprocal device for pulses, which have a broadband spectral signature. To demonstrate this, we excite our metamaterial with half-sine shaped pulses closely mimicking a pulse of amplitude 0.04 rad and duration 100 ms, either from the left or right edge. In the reciprocal case $\alpha = 0$, the response is strictly the same regardless of the excitation point (Fig. 4a–c). The pulses propagate across

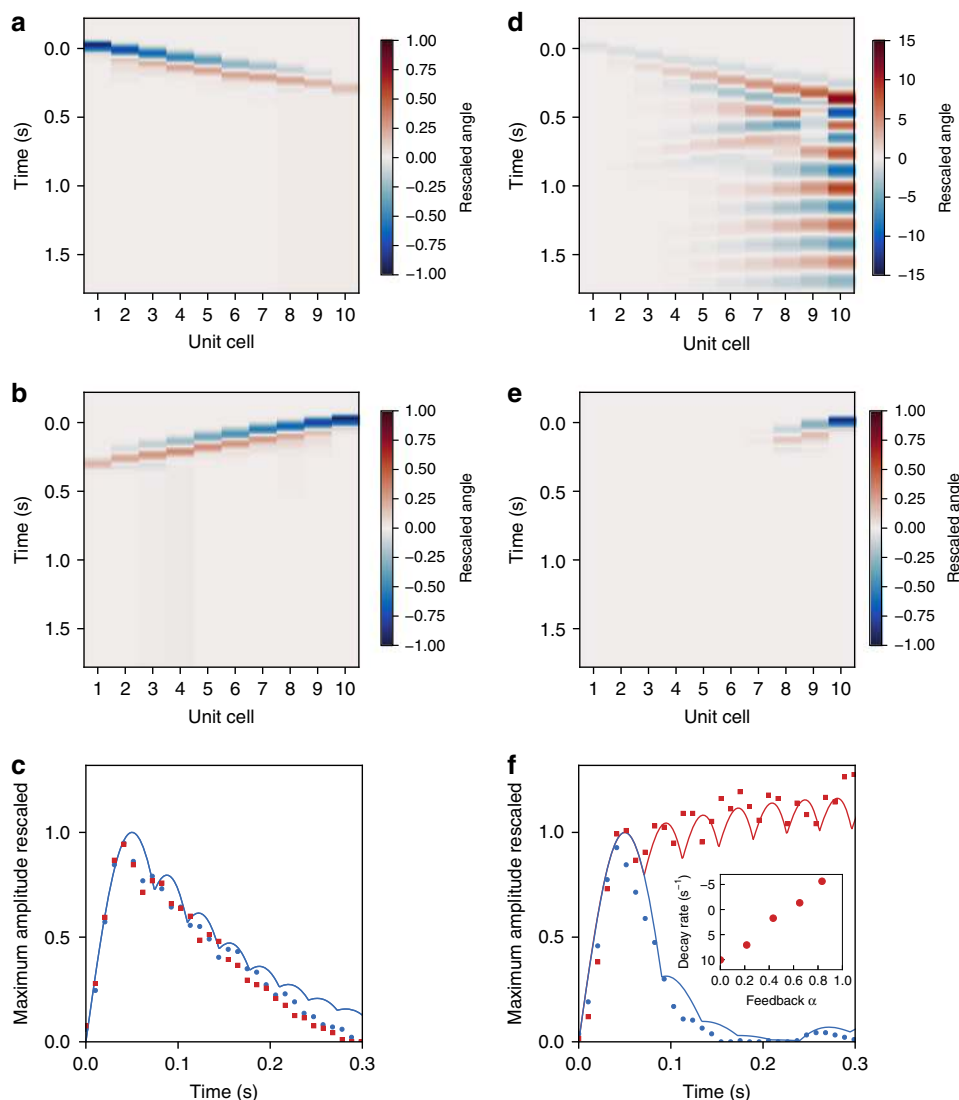


Fig. 4 Unidirectional pulse amplification. **a–e** Contour plots of the angular displacement vs. space coordinate and time for a feedback parameter $\alpha = 0$ (**ab**) and $\alpha = 0.62$ (**de**), upon pulse excitation on the left (**ad**) and right (**be**) edge of the metamaterial. (**c**) Instantaneous maximum magnitude of the propagation pulse vs. time for a feedback parameter $\alpha = 0$ (**c**) and $\alpha = 0.62$ (**f**). The points correspond to the experimental data, the thin solid lines to the numerical model without any fit parameters. (**f**-inset) Decay rate δ derived from exponential fits of the form $\exp(-\delta t)$ on the maximum amplitude of pulses propagating from left to right for different values of the feedback parameter. See also Supplementary Video 2

the metamaterial, reach the opposite edge, and rapidly attenuate upon reflection. After a short transient and before the first reflection, the pulse amplitude decreases (Fig. 4c). By contrast, in the nonreciprocal case $\alpha = 0.62$ (Fig. 4d–f), the pulse attenuates strongly when excited from the right and is amplified when excited from the left. In the latter case, the pulse reaches the right edge of the robotic metamaterial and remains localized in the vicinity of this edge from where it slowly decays in time (see Supplementary Fig. 7). To quantify the pulse attenuation, we restrict our attention to the propagation before the first reflection (Fig. 4c, f). We find that the unidirectional amplification is controlled by the level of feedback α : the signal is amplified (attenuated) for $\alpha > 0.5$ ($\alpha < 0.5$) (see Fig. 4f—inset). These observations are in qualitative agreement with the behavior of the Green’s function of Eq. (1) discussed above.

Discussion

To conclude, we have created a class of robotic mechanical metamaterials that are embedded with nonreciprocal interactions

through local control loops. As a result, they feature a unique type of wave phenomena, which show spatial asymmetry of standing waves at all frequencies, leading to an unprecedented broadband giant level of non-reciprocity, and which exhibit unidirectional amplification of pulses. As opposed to existing metamaterials by using nonlinearities or active components, where the non-reciprocal effects tend to be suppressed by attenuation for large system sizes³¹, the key new feature here is that nonreciprocal waves are unidirectionally amplified, which guarantees robustness against attenuation. Nonreciprocal robotic metamaterials could be used to extract mechanical energy, allowing energy to flow away from a source while preventing energy to flow back to it. Therefore, we envision that further developments on non-reciprocal robotic metamaterials will provide new vistas for applications where unidirectional transmission of energy is useful, e.g., for communication and sensing^{3,7,9,20,33,34}, shock and vibration damping, and energy harvesting^{13,17,21,35–37}. Our study opens up a plethora of future research directions, e.g., the investigation of odd elasticity²², instabilities³⁸, and non-Hermitian physics^{23–28,39}. Finally, we believe that recent

developments in stimuli-responsive materials^{40,41} and robotics—via MEMS or graphene origami^{19,42}—will allow to embed active control in materials as a smaller scale, for higher dimensions, and beyond rotational degrees of freedom—e.g., for acoustics, flexural waves, and quantum systems.

Methods

Mass-and-spring model with nonreciprocal springs. In this section, we describe the mass-and-spring model with nonreciprocal interactions discussed in Fig. 1 of the main text and derive its continuum limit (Eq. (1) of the main text). We then calculate its solutions in the frequency domain as well as its Green's function.

Consider a mass-and-spring model, where all masses m are equal and all the springs are equivalent and of rest-length p . Newton's second law reads

$$m \frac{d^2 u_j}{dt^2} = F_{j-1 \rightarrow j} + F_{j+1 \rightarrow j}, \quad (2)$$

where u_j is the displacement of mass j and $F_{j-1 \rightarrow j} = k_{j-1 \rightarrow j}(u_{j-1} - u_j)$ ($F_{j+1 \rightarrow j} = k_{j+1 \rightarrow j}(u_{j+1} - u_j)$) is the force exerted by the spring between masses $j-1$ ($j+1$) and j . In an ordinary reciprocal system, $k_{j-1 \rightarrow j} = k_{j \rightarrow j-1} = k$, and the right-hand side of Eq. (2) becomes $k(u_{j-1} + u_{j+1} - 2u_j)$. By contrast, here we consider a special case where the springs are nonreciprocal $k_{j-1 \rightarrow j} = k(1 + \epsilon) \neq k_{j \rightarrow j-1} = k(1 - \epsilon)$. In such a model, Newton's action–reaction third law is broken, which means that in practice one needs to add local momentum at each site j to realize such a system. The equation of motion for mass j becomes

$$m \frac{d^2 u_j}{dt^2} + k(1 + \epsilon)(u_j - u_{j-1}) + k(1 - \epsilon)(u_j - u_{j+1}) = 0. \quad (3)$$

In order to study the behavior of such a system, it is useful to consider the continuum limit, given by $u_j \rightarrow u(x)$ and $u_{j \pm 1} \rightarrow u(x) \pm p(du/dx) + p^2/2(d^2u/dx^2)$, and which then leads to Eq. (1) of the main text. In the case of a reciprocal system ($\epsilon = 0$), Eq. (1) becomes the wave equation, which admits dispersion-free mechanical waves of group and phase velocity c . For arbitrary ($\epsilon \neq 0$), Eq. (1) is analogous to the Telegrapher's equation^{43,44}, but where time and space have been interchanged.

If we assume that the medium is infinite, the Floquet–Bloch theorem predicts that plane wave solutions of the form $u(x, t) = u_0 \exp(i\omega t - qx)$ are solutions of Eq. (1), where ω is the radial frequency and q the wave vector. By inserting this expression in Eq. (1), we obtain the following dispersion relation

$$-\frac{\omega^2}{c^2} + q^2 - \frac{2\epsilon i}{p} q = 0. \quad (4)$$

Therefore, for a given ω , solutions are of the form $u(x, t) = \exp(i\omega t) \exp(-iqx)$, where $q_{\pm} = \frac{i}{p} \left(\epsilon \pm \sqrt{\epsilon^2 - \frac{p^2 \omega^2}{c^2}} \right)$. This result is discussed in the main text.

We calculate the Green's function of Eq. (1) by using Fourier–Laplace transforms (see Supplementary Note 1) and find

$$u(x, t) = \frac{e^{\epsilon x/p}}{2} \Theta \left(t - \frac{|x|}{c} \right) \left(J_0 \left(\epsilon \frac{\sqrt{c^2 t^2 - |x|^2}}{p} \right) - \frac{(ct - |x|)^2}{c^2 t^2 - |x|^2} J_2 \left(\epsilon \frac{\sqrt{c^2 t^2 - |x|^2}}{p} \right) \right), \quad (5)$$

where Θ is the Heaviside step function and where J_k are Bessel functions of the first kind. This solution predicts that a pulse in $x = 0$ at time $t = 0$ leads to an asymmetric step function propagating with an exponentially increasing (decreasing) amplitude (see Fig. 1c of the main text) for forward (backward) propagation. In addition, we can rationalize this behavior by restricting our attention to the moving frame, that is, $|x| = ct$, we find

$$u_{\text{movingframe}}(t) = \begin{cases} \frac{1}{2} \text{expect}/p & \text{for } x > 0 \\ \frac{1}{2} \exp - \epsilon ct/p & \text{for } x < 0, \end{cases} \quad (6)$$

which is discussed in the main text. Note that in the limit $\epsilon \rightarrow 0$, Eq. (1) becomes the 1D wave equation. Our solution is consistent with this limit, since $J_0(0) = 1$ and $J_2(0) = 0$, Eq. (5) becomes the well-known Green's function for the 1D wave equation⁴⁵ $u(x, t) = \frac{1}{2} \Theta \left(t - \frac{|x|}{c} \right)$.

Realization of the robotic mechanical metamaterial. The 1D robotic mechanical metamaterial shown in Fig. 2a of the main text consists of a chain of mechanically coupled oscillators, each of which is combined with a minimal robotic system. These robotic unit cells, of dimensions 54 mm × 54 mm × 90 mm, are exact duplicates of each other. In this section, we provide details about the mechanical, electromechanical, and software characteristics of these building blocks.

Each oscillator is made up of (i) a 3D printed arm (ABS, red part in Supplementary Fig. 2a); (ii) two stainless-steel bolts and four nuts (M6) fastened to each side of the arm; (iii) the shaft of a coreless DC motor (Motraxx CL1628, blue part in Supplementary Fig. 2a); (iv) a custom-made aluminum shaft extension connected to the disk of an optical angular encoder (Broadcom HEDR-55L2-BY09, yellow part in Supplementary Fig. 2a). The total moment of inertia

$J = 27.550 \pm 0.08 \mu\text{g m}^2$ and the damping coefficient $\gamma = 31.16 \pm 2.34 \mu\text{N s m}$ have been determined via independent calibration measurements.

The oscillators are mechanically coupled to each other by two soft elastic beams made of vinylpolysiloxane (Elite double 8, Young's modulus $E = 0.25 \text{ MPa}$). The elastic beams are pre-stretched by 30% to avoid buckling when arms extremities come closer to each other. The structure of the elastic beams, shown in Supplementary Fig. 2b, c, is laser cut from a 2-mm thin cast sheet. The empty squares of the elastic structure are used to attach the elastic beam to the square-shaped protuberances of the oscillator arms. The square shape prevents any rotation of the elastic structure around its connection. In between each square, the elastic beam has an elongated hexagonal shape, with a maximum thickness of 6 mm and a minimum thickness of 1 mm.

When the oscillators rotate, the elastic beams can stretch and contract, with the deformations localized at the thin necks. Since the squared connection does not allow any sliding of the elastic structure on the oscillator's arm, the elastic beam also undergoes bending deformations localized at the think necks. We describe the effect of these deformations on the energy of the system as follows: when the rotations of neighboring oscillators θ_L and θ_R are symmetrical ($\theta_L = -\theta_R$), the elastic links primarily stretch/contract, and when the deformation of the neighboring oscillators is antisymmetrical ($\theta_L = \theta_R$), the links primarily bend. The energy of these two deformation modes can be expressed as $(C/2)(\theta_L - \theta_R)^2$ for the symmetrical mode and $(C'/2)(\theta_L + \theta_R)^2$ for the antisymmetrical mode. The torsional stiffnesses associated with these two deformation modes C and C' differ. We optimized the geometry such that $C' = C$ (Supplementary Fig. 2c), see below for calibration. Note that the geometry to guarantee that $C' = C$ introduces unavoidable spurious vibrational effects, which are hard to control and which effectively reduce the stiffness C at large frequencies ($>3 \text{ Hz}$, see Supplementary Fig. 5d).

The control system is made up of (i) an angular sensor (Broadcom HEDR-55L2-BY09, yellow part in Supplementary Fig. 2a); (ii) a coreless DC motor (Motraxx CL1628, blue part in Supplementary Fig. 2a) embedded in a cylindrical heatsink (in dark gray in Supplementary Fig. 2a); (iii) a microcontroller (Arduino ATmega32U4, integrated circuit in Supplementary Fig. 2a); (iv) a UART connection receiving the angular position of the right unit cell and transmitting its own angular position to the left unit cell.

Angular encoder: The angular sensor measures the position of the oscillator with a precision of 14000 PPR (pulse per revolution), which translates into a precision of $4 \times 10^{-4} \text{ rad}$.

Microcontroller: The microcontroller digitizes the encoder's signal with an angular resolution of $4 \times 10^{-4} \text{ rad}$ at a rate of 100 Hz and collects the angular position of the unit cell's right neighbor through a serial protocol (UART connection) at a rate of 100 Hz. From a 9-bit timer, the microcontroller also builds up a pulse-width modulation (PWM) signal, to control the motor. The microcontroller is integrated to a custom-made electronic board that ensures power conversion and wiring to the motor, encoder, and the neighboring unit cells. The firmware of the microcontroller is uploaded from an external computer by serial communication (USB port). Although the microcontroller is not required to be connected to an external computer to function, if required, data can also be sent to an external computer (rate 100 Hz) via the same serial communication.

DC motor: In order to apply a given torque, the motor is controlled by a PWM signal. The PWM signal is sent to the motor and controls the generated torque with a resolution of 0.008 mN m, up to a maximum torque of $\tau = 3.92 \text{ mN m}$. Note that this maximum explains the saturation of the effective stiffness $C_{R \rightarrow L}$ for large values of the feedback parameter α in Fig. 2d in the main text.

Software: The basic algorithm of the software is depicted in Fig. 2c of the main text and runs continuously at a rate of 100 Hz. Each microcontroller collects the instantaneous angular position measures of its own angular sensor θ_L as well as the instantaneous angular position θ_R of the right neighbor. From those two signals, the microcontroller is programmed to output a PWM signal proportional to $g(\theta_L - \theta_R)$, where the constant g is a tunable gain parameter. This signal drives the DC motor, which leads to a torque proportional to $g(\theta_L - \theta_R)$, see below for calibration.

Calibration and measurements. In order to perform measurements, the robotic metamaterial is actuated by a servomotor (Hitec D930DW, see Supplementary Fig. 3) controlled via a microcontroller (Arduino Mega 2560), interfaced to an external computer. The servomotor can be attached on either side of the setup and is mechanically connected to one oscillator via two green elastic structures (rectangular shape, 6-mm thick, Elite double 32, Young's modulus $E = 1 \text{ MPa}$, resulting in a torsional stiffness 27.4 mN m/rad, see Supplementary Fig. 4). These two elastic beams are sufficiently soft to ensure free rotations of the servomotor and negligible friction.

The stiffness measurements shown in Fig. 2d of the main text have been performed on two building blocks. The configuration of the setup is sketched in Supplementary Fig. 4a (see also Supplementary Fig. 5a). The left (right) oscillator was attached to a load cell (Instron 2530-5 N, resolution of 0.005 N, sampling frequency of 500 Hz) at a fixed position $\theta_L = 0$ ($\theta_R = 0$), allowing us to measure the torque, $\tau_{R \rightarrow L}$ ($\tau_{L \rightarrow R}$). The right (left) oscillator was driven by the servomotor, imposing an oscillatory angular displacement θ_R (θ_L) at the frequency 0.1 Hz and amplitude 0.13 rad.

9. Fleury, R., Sounas, D. L., Sieck, C. F., Haberman, M. R. & Alù, A. Sound isolation and giant linear nonreciprocity in a compact acoustic circulator. *Science* **343**, 516–519 (2014).
10. Peano, V., Houde, M., Marquardt, F. & Clerk, A. A. Topological quantum fluctuations and traveling wave amplifiers. *Phys. Rev. X* **6**, 041026 (2016).
11. Lau, H. K. & Clerk, A. A. Fundamental limits and non-reciprocal approaches in non-hermitian quantum sensing. *Nat. Commun.* **9**, 4320 (2018).
12. Nash, L. M. et al. Topological mechanics of gyroscopic metamaterials. *Proc. Natl Acad. Sci. USA* **112**, 14495–14500 (2015).
13. Coulais, C., Sounas, D. & Alù, A. Static non-reciprocity in mechanical metamaterials. *Nature* **542**, 461–464 (2017).
14. Sounas, D. L., Soric, J. & Alù, A. Broadband passive isolators based on coupled nonlinear resonances. *Nat. Electron* **1**, 113–119 (2018).
15. Hadad, Y., Soric, J. C. & Alù, A. Breaking temporal symmetries for emission and absorption. *Proc. Natl Acad. Sci. USA* **113**, 3471–3475 (2016).
16. Souslov, A., van Zuiden, B. C., Bartolo, D. & Vitelli, V. Topological sound in active-liquid metamaterials. *Nat. Phys.* **13**, 1091–1094 (2017).
17. Wang, Y. et al. Observation of nonreciprocal wave propagation in a dynamic phononic lattice. *Phys. Rev. Lett.* **121**, 194301 (2018).
18. McEvoy, M. A. & Correll, N. Materials science. materials that couple sensing, actuation, computation, and communication. *Science* **347**, 1261689 (2015).
19. Miskin, M. Z. et al. Graphene-based bimorphs for micron-sized, autonomous origami machines. *Proc. Natl Acad. Sci. USA* **115**, 466–470 (2018).
20. Rivet, E. et al. Constant-pressure sound waves in non-hermitian disordered media. *Nat. Phys.* **14**, 942–947 (2018).
21. Trainiti, G. et al. Time-periodic stiffness modulation in elastic metamaterials for selective wave filtering: theory and experiment. *Phys. Rev. Lett.* **122**, 124301 (2019).
22. Scheibner, C. et al. Odd elasticity. Preprint at: <http://arxiv.org/abs/1902.07760> (2019).
23. Martínez Alvarez, V. M., Barrios Vargas, J. E. & Foa Torres, L. E. F. Non-hermitian robust edge states in one dimension: anomalous localization and eigenspace condensation at exceptional points. *Phys. Rev. B* **97**, 121401 (2018).
24. Yao, S. & Wang, Z. Edge states and topological invariants of non-hermitian systems. *Phys. Rev. Lett.* **121**, 086803 (2018).
25. Lee, C. H. & Thomale, R. Anatomy of skin modes and topology in non-hermitian systems. *Phys. Rev. B* **99**, 201103(R) (2019).
26. Borgnia, D. S., Kruchkov, A. J. & Slager, R.-J. Non-hermitian boundary modes. Preprint at: <http://arxiv.org/abs/1902.07217> (2019).
27. Helbig, T. et al. Observation of bulk boundary correspondence breakdown in topological circuits. Preprint at: <http://arxiv.org/abs/1907.11562> (2019).
28. Xiao, L. et al. Observation of non-hermitian bulk-boundary correspondence in quantum dynamics. Preprint at: <http://arxiv.org/abs/1907.12566> (2019).
29. Kittel, C. *Phonons I. Crystal Vibrations*. Book section 4 (Wiley, New York, 1976).
30. Huber, S. D. Topological mechanics. *Nat. Phys.* **12**, 621–623 (2016).
31. Coulais, C., Kettenis, C. & van Hecke, M. A characteristic lengthscale causes anomalous size effects and boundary programmability in mechanical metamaterials. *Nat. Phys.* **14**, 40–44 (2018).
32. Frenzel, T., Kadic, M. & Wegener, M. Three-dimensional mechanical metamaterials with a twist. *Science* **358**, 1072–1074 (2017).
33. Khanikaev, A. B., Fleury, R., Mousavi, S. H. & Alù, A. Topologically robust sound propagation in an angular-momentum-biased graphene-like resonator lattice. *Nat. Commun.* **6**, 8260 (2015).
34. Mitchell, N. P., Nash, L. M., Hexner, D., Turner, A. M. & Irvine, W. T. M. Amorphous topological insulators constructed from random point sets. *Nat. Phys.* **14**, 380–385 (2018).
35. Raney, J. R. et al. Stable propagation of mechanical signals in soft media using stored elastic energy. *Proc. Natl Acad. Sci. USA* **113**, 9722–9727 (2016).
36. Hwang, M. & Arrieta, A. F. Input-independent energy harvesting in bistable lattices from transition waves. *Sci. Rep.* **8**, 3630 (2018).
37. Gonella, S., To, A. C. & Liu, W. K. Interplay between phononic bandgaps and piezoelectric microstructures for energy harvesting. *J. Mech. Phys. Solids* **57**, 621–633 (2009).
38. Bertoldi, K., Vitelli, V., Christensen, J. & van Hecke, M. Flexible mechanical metamaterials. *Nat. Rev. Mater.* **2**, 17066 (2017).
39. El-Ganainy, R. et al. Non-hermitian physics and pt symmetry. *Nat. Phys.* **14**, 11–19 (2018).
40. White, T. J. & Broer, D. J. Programmable and adaptive mechanics with liquid crystal polymer networks and elastomers. *Nat. Mater.* **14**, 1087–1098 (2015).
41. Kim, Y., Yuk, H., Zhao, R., Chester, S. A. & Zhao, X. Printing ferromagnetic domains for untethered fast-transforming soft materials. *Nature* **558**, 274–279 (2018).
42. Rogers, J., Huang, Y., Schmidt, O. G. & Gracias, D. H. Origami mems and nems. *MRS Bull.* **41**, 123–129 (2016).
43. Goldstein, S. On diffusion by discontinuous movements, and on the telegraph equation. *Q. J. Mech. Appl. Math.* **17**, 129–156 (1951).
44. Masoliver, J. & Weiss, G. Finite-velocity diffusion. *Eur. J. Phys.* **4**, 190–196 (1996).
45. Watanabe, K. *Integral Transform Techniques for Green's Function*. (Springer: Switzerland, 2014).
46. Guckenheimer, J. & Holmes, P. J. *Nonlinear Oscillations, Dynamical Systems, and Bifurcations of Vector Fields*. (Springer-Verlag, New York, 1983).

Acknowledgements

We thank D. Giesen, G. Hardeman, U. van Hes, T. Walstra, and T. Weijers for their skilful technical assistance. We are grateful to A. Alù, Y. Hadad, and J. van Wezel for their insightful discussions. C.C. acknowledges funding from the Netherlands Organization for Scientific Research (NWO) VENI grant No. NWO-680-47-445.

Author contributions

M.B., E.L., and C.C. designed the research. M.B. and C.C. designed the experimental setup. M.B. and X.L. conducted the experiments and performed the data analysis, and M. B., E.L., and C.C. contributed to the theoretical model. M.B. and C.C. wrote the paper with input from E.L.

Competing interests

The authors declare no competing interests.

Additional information

Supplementary information is available for this paper at <https://doi.org/10.1038/s41467-019-12599-3>.

Correspondence and requests for materials should be addressed to C.C.

Peer review information *Nature Communications* thanks the anonymous reviewers for their contribution to the peer review of this work. Peer reviewer reports are available.

Reprints and permission information is available at <http://www.nature.com/reprints>

Publisher's note Springer Nature remains neutral with regard to jurisdictional claims in published maps and institutional affiliations.



Open Access This article is licensed under a Creative Commons Attribution 4.0 International License, which permits use, sharing, adaptation, distribution and reproduction in any medium or format, as long as you give appropriate credit to the original author(s) and the source, provide a link to the Creative Commons license, and indicate if changes were made. The images or other third party material in this article are included in the article's Creative Commons license, unless indicated otherwise in a credit line to the material. If material is not included in the article's Creative Commons license and your intended use is not permitted by statutory regulation or exceeds the permitted use, you will need to obtain permission directly from the copyright holder. To view a copy of this license, visit <http://creativecommons.org/licenses/by/4.0/>.

© The Author(s) 2019